## nature chemistry

**Article** 

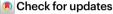
https://doi.org/10.1038/s41557-023-01285-z

## Single-cell multimodal imaging uncovers energy conversion pathways in biohybrids

Received: 17 August 2022

Accepted: 28 June 2023

Published online: 27 July 2023



Bing Fu 1,5,9, Xianwen Mao1,6,9, Youngchan Park 1, Zhiheng Zhao1, Tianlei Yan 1, Won Jung<sup>1,7</sup>, Danielle H. Francis<sup>1,8</sup>, Wenjie Li 1, Brooke Pian 2, Farshid Salimijazi<sup>2</sup>, Mokshin Suri<sup>3</sup>, Tobias Hanrath • A. Buz Barstow • & Peng Chen **©**<sup>1</sup>⊠

Microbe-semiconductor biohybrids, which integrate microbial enzymatic synthesis with the light-harvesting capabilities of inorganic semiconductors, have emerged as promising solar-to-chemical conversion systems. Improving the electron transport at the nano-bio interface and inside cells is important for boosting conversion efficiencies, yet the underlying mechanism is challenging to study by bulk measurements owing to the heterogeneities of both constituents. Here we develop a generalizable, quantitative multimodal microscopy platform that combines multi-channel optical imaging and photocurrent mapping to probe such biohybrids down to single- to sub-cell/particle levels. We uncover and differentiate the critical roles of different hydrogenases in the lithoautotrophic bacterium Ralstonia eutropha for bioplastic formation, discover this bacterium's surprisingly large nanoampere-level electron-uptake capability, and dissect the cross-membrane electron-transport pathways. This imaging platform, and the associated analytical framework, can uncover electron-transport mechanisms in various types of biohybrid, and potentially offers a means to use and engineer R. eutropha for efficient chemical production coupled with photocatalytic materials.

Utilizing solar energy to efficiently synthesize higher-value chemicals from earth-abundant molecules such as CO<sub>2</sub> remains a long-standing challenge. Microbe-semiconductor biohybrids have emerged as promising systems to address this challenge by combining the high lightharvesting efficiencies of inorganic semiconductors with the capacity of microbes to orchestrate complex chemical transformations<sup>1-6</sup>. In the 'decoupled biohybrids' (Fig. 1a, top), semiconductor-based photovoltaics power water electrolysis to generate H<sub>2</sub>, which is subsequently fed to lithoautotrophic bacteria (for example, Ralstonia eutropha and

Methanosarcina barkeri) to fix CO<sub>2</sub> to value-added chemicals (for example, biomass, isopropanol and methane)<sup>7,8</sup>. In 'integrated biohybrids' (Fig. 1a, bottom), the microbes (for example, Sporomusa ovata, Moorella thermoacetica and Saccharomyces cerevisiae) are directly interfaced with semiconductor photoelectrodes or photocatalysts, where photogenerated electrons are taken up by the microbes to drive downstream biosynthesis of acetic acid, methane, shikimic acid, polymers and so on  $9^{-12}$ .

Key to fully exploiting such biohybrid systems is the engineering of semiconductors and bacteria on the basis of mechanistic, quantitative

Department of Chemistry and Chemical Biology, Cornell University, Ithaca, NY, USA. Department of Biological and Environmental Engineering, Cornell University, Ithaca, NY, USA. 3Department of Materials Science and Engineering, Cornell University, Ithaca, NY, USA. 4Robert F. Smith School of Chemical and Biomolecular Engineering, Cornell University, Ithaca, NY, USA. 5 Present address: Department of Biomedical Engineering, City University of Hong Kong, Hong Kong, China. <sup>6</sup>Present address: Department of Materials Science and Engineering, Institute of Functional Intelligent Materials, and Centre for Advanced 2D Materials, National University of Singapore, Singapore, Singapore. <sup>7</sup>Present address: Department of Chemistry and Chemical Biology, Harvard University, Cambridge, MA, USA. 8 Present address: Friends School of Baltimore, Baltimore, MD, USA. 9 These authors contributed equally: Bing Fu, Xianwen Mao. Me-mail: pc252@cornell.edu

guidance for improving energy conversion efficiencies. Although bulk-level studies have provided important insights<sup>7,10,13–16</sup>, their interpretations are complicated by the ubiquitous heterogeneities of microbial cells in gene expression<sup>17</sup> and of semiconductor particles in photocatalytic activity<sup>18,19</sup>. Such heterogeneities demand quantitative measurements at the single- and sub-cell/particle levels.

In this Article we develop a generalizable, multimodal imaging approach, combining multi-channel fluorescence microscopy and photoelectrochemical current mapping, to interrogate the players and energy conversion pathways in microbe-semiconductor biohybrids for CO<sub>2</sub> fixation down to single-molecule, single-cell and single/ sub-particle level (Fig. 1b). We focus on the lithoautotrophic Gramnegative bacterium Ralstonia eutropha (a.k.a. Cupriavidus necator), which was previously used in decoupled biohybrids using H<sub>2</sub> as the sole energy source to fix CO<sub>2</sub> into the bioplastic polyhydroxybutyrate (PHB)<sup>20</sup>. We dissect the different roles of membrane-bound and soluble hydrogenases towards PHB formation in the cell grown under H<sub>2</sub> and CO<sub>2</sub>. We discover a surprisingly large, nanoampere-level electron-uptake capability of R. eutropha from semiconductor photoelectrodes with different energy levels. We further show that this large interfacial electron transport is dominantly mediated by species other than H<sub>2</sub>, yet hydrogenases play critical roles in sustaining these photoelectrochemical currents. These findings raise the possibilities of using R. eutropha in both decoupled and integrated biohybrids and provide quantitative insights to guide microbial engineering for enhanced energy conversion.

#### **Results and discussion**

#### Role of hydrogenases in bioplastic production

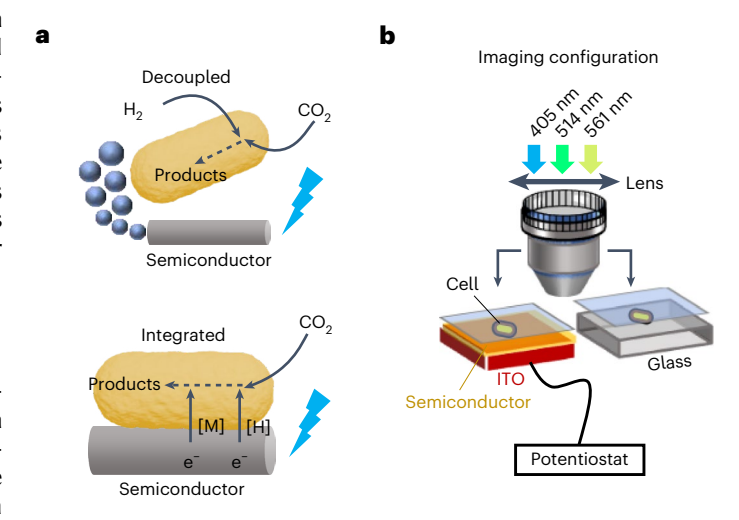
 $R.\ eutropha$  uses two types of hydrogenase to metabolize  $H_2$  (Supplementary Fig. 1): a membrane-bound hydrogenase (MBH), which comprises HoxGKZ subunits and is known to deliver electrons to the respiratory chain that generates a proton gradient across the membrane for producing ATP, and a cytosolic soluble hydrogenase (SH), which comprises HoxFUYHI subunits and generates NADH for downstream biosynthesis  $^{21-23}$ . To probe their roles in bioplastic production under lithoautotrophic growth, we examined their cellular concentrations in relation to cellular PHB production at the single-cell level using optical imaging (Fig. 1b).

To visualize PHB, we tagged PhaP1, a PHB granule-association protein<sup>24</sup>, or PhaC, a PHB synthase<sup>25</sup>, with the yellow fluorescent protein mVenus (mV) at their respective chromosomal loci, enabling their imaging down to single-molecule sensitivity (Supplementary Sections 1.2–1.4). Both proteins decorate PHB granules<sup>26</sup>, and their expression levels also scale with the amount of PHB in bulk cultures<sup>27</sup>.

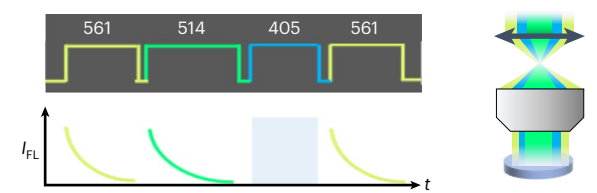
Fig. 1| Microbe-semiconductor biohybrids and multimodal imaging platform. a, Decoupled and integrated biohybrids for energy conversion. [H]:  $H^+/H_2$  as the redox mediator, where  $H_2$  can be generated by electrocatalysts or photocatalysts; [M]: other redox mediators. b, Multimodal imaging platform (details are provided in Supplementary Sections 1.3-1.5), consisting of a (photoelectrochemical) microfluidic cell on an epifluorescence microscope with multiple, modulated lasers for wide-field and/or focused excitation. Indium tin oxide (ITO) connected to a potentiostat is used as the working electrode for photoelectrochemical current mapping. A 405-nm laser is used for photoactivating PAmC1 and/or exciting the semiconductors, a 514-nm laser for exciting mV and a 561-nm laser for exciting mC and the photoactivated PAmC1. c, Imaging mode I: multi-channel wide-field fluorescence imaging to quantify fluorescent-tagged proteins in single cells, showing the timing (t) of lasers (top left), the protein fluorescence  $I_{FL}$  (bottom left) and the laser excitation geometry (right). d, Mode II: super-resolution single-molecule tracking by stroboscopic fluorescence imaging. Left: schematic position trajectories in a cell. r, displacement; AOTF, acoustic-optic tunable filter. e, Mode III: focused laser illumination to probe single-spot photoelectrochemical currents on single cells in contact with a semiconductor film (i) or with single semiconductor particles (ii and iii).  $i_{ph}$ , photocurrent.

We first imaged PhaP1<sup>mV</sup> or PhaC<sup>mV</sup> in *R. eutropha* grown with fructose as the carbon source (that is, non-adapted condition). These cells are micrometre-long and rod-shaped, with PHB granules clearly visible in bright-field transmission images (Fig. 2a). Under wide-field fluorescence imaging (Fig. 1c, mode I-i), PhaP1<sup>mV</sup> and PhaC<sup>mV</sup> expectedly colocalize with PHB granules (Fig. 2b and Supplementary Fig. 7b–e), confirming the function and integrity of the tagged proteins (Supplementary Section 2). Furthermore, the PhaP1 and PhaC copy numbers of individual cells, determined from wide-field fluorescence imaging, scale linearly with PHB granule sizes (Fig. 2i and Supplementary Fig. 10g), validating PhaP1/PhaC as quantitative reporters for PHB level. Because of its higher copy numbers and stronger linear correlation with granule sizes than PhaC, we use PhaP1 as the PHB reporter in the following.

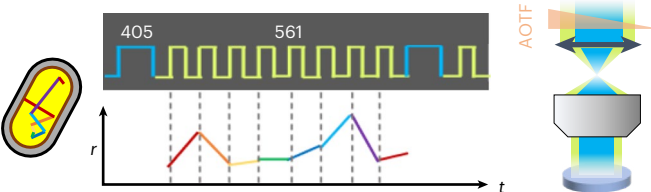
We then quantified PHB in *R. eutropha* cells lithoautotrophically grown with H<sub>2</sub>, CO<sub>2</sub> and air (that is, the adapted condition; Methods



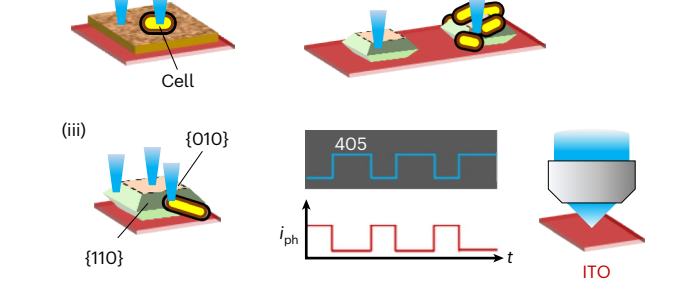
Mode I: multi-channel imaging (i. 1-colour; ii. 2-colour; iii. 3-channel)



**d** Mode II: single-molecule super-resolution imaging and tracking



Mode III: single-cell and sub-particle photocurrent imaging



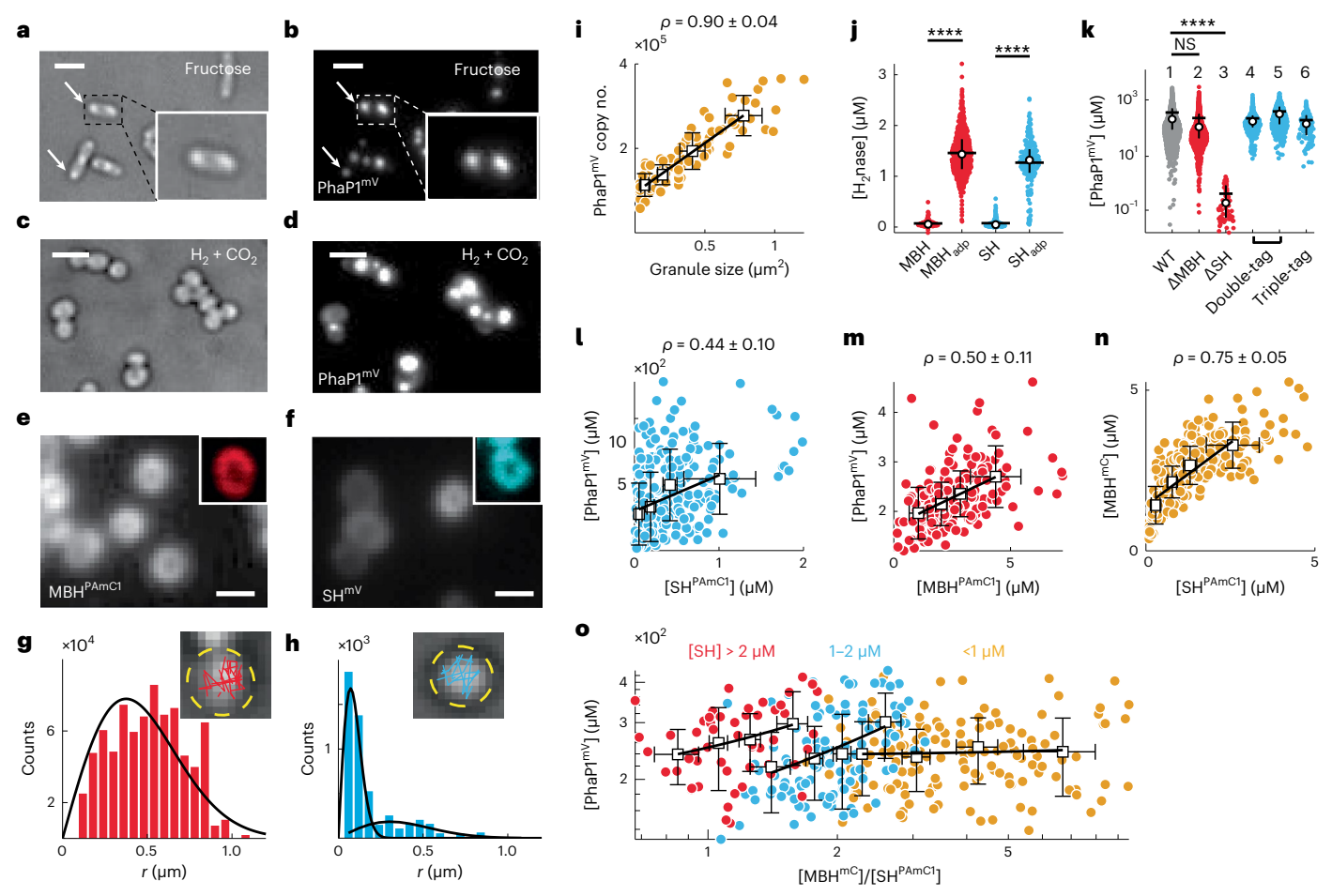


Fig. 2 | Roles of hydrogenases in bioplastic formation under lithoautotrophic growth. a, Bright-field transmission image of PhaP1<sup>mV</sup> R. eutropha cells grown with fructose (that is, non-adapted). PHB granules appear as punctate spots, two of which are marked by arrows. b, Wide-field fluorescence image corresponding to a, showing the PhaP1<sup>mV</sup> decorating PHB granules. c,d, Same as a,b, but for PhaP1<sup>mV</sup> *R. eutropha* cells grown with  $H_2$  and  $CO_2$  (that is, adapted). Scale bars,  $2 \mu m$  (**a**-**d**).  $\textbf{e,f,} \ \text{Wide-field fluorescence images of adapted MBH}^{PAmC1}_{HoxG}(\textbf{e}) \ \text{and SH}^{mV}_{HoxY}(\textbf{f}) \ \text{cells.}$ Insets: false-coloured confocal fluorescence images. Scale bars, 1 µm. g,h, Cell-confinement-effect-deconvoluted displacement length r distributions of  $MBH_{HoxG}^{PAmC1}(\mathbf{g})$  and  $SH_{HoxY}^{PAmC1}(\mathbf{h})$  from single-molecule tracking (Supplementary Section 7). Black lines: fitted one (g) or two (h) Brownian diffusion state displacement distributions. Insets: representative single-molecule tracking trajectories (red/blue lines) overlaid on the transmission image of a cell. Yellow dashed lines: cell contours. i, Correlation between PhaP1<sup>mV</sup> copy number and PHB granule size in single non-adapted cells (yellow dots). Black open squares are binned and averaged results. Across individual bins there are approximately equal numbers of data points to be statistically equivalent. Black line: linear fit as a guide

to the eye (same for  $\mathbf{l} - \mathbf{o}$ ).  $\rho$ , Pearson's correlation coefficient with 95% confidence interval calculated from the original data points. n = 95 cells. **j**, Cellular concentrations of MBH  $^{mV}_{HoxG}$  and SH  $^{mV}_{HoxY}$  in non-adapted (columns 1 and 3; sample size n = 126 and 589) and adapted cells (columns 2 and 4; sample size n = 177 and 194). Two-sided t-test, \*\*\*\*P < 0.0001. **k**, Cellular PhaP1<sup>mV</sup> concentrations in different adapted strains. Column 1: PhaP1 $^{mV}$ , sample size n = 2,417; column 2: PhaP1<sup>mV</sup>,  $\triangle$ MBH( $\triangle$ hoxG), n = 1.561; column 3: PhaP1<sup>mV</sup>,  $\triangle$ SH( $\triangle$ hoxY), n = 66; column 4:  $MBH_{HoxG}^{PAmC1}$ ,  $PhaP1^{mV}$ , n = 513; column 5:  $SH_{HoxY}^{PAmC1}$ ,  $PhaP1^{mV}$ , n = 579; column 6:  $\mathsf{MBH}^{\mathsf{mC}}_{\mathsf{HoxG}}, \mathsf{SH}^{\mathsf{PAmC1}}_{\mathsf{HoxY}}, \mathsf{PhaP1}^{\mathsf{mV}}, n = 130.\,\mathsf{NS}, \mathsf{not}\,\mathsf{significant}.\,\mathsf{Two\text{-}sided}\,t\text{-}\mathsf{test},$ \*\*\*\*P < 0.0001. In **j** and **k**, white circles denote the median, horizontal black lines the mean, vertical black lines the 25% to 75% quantile. **I-n**, Cellular protein concentration correlations in adapted single cells (coloured dots) between PhaP1<sup>mV</sup> and SH<sup>PAmC1</sup><sub>HoxY</sub>, n = 243 cells (I), PhaP1<sup>mV</sup> and MBH<sup>PAmC1</sup><sub>HoxG</sub>, n = 190 cells (**m**),  $MBH_{HoxG}^{mC}$  and  $SH_{HoxY}^{PAmC1}$ , n = 313 cells (**n**). **o**, Cellular PhaP1<sup>mV</sup> concentration versus  $[MBH^{mC}_{HoxG}]/[SH^{PAmCI}_{HoxY}] \ in \ single \ adapted \ cells \ (coloured \ dots), sorted \ into \ three \ details \ (coloured \ dots), sorted \ into \ into \ dots), sorted \ into \ into \ into \ dots), sorted \ into \ i$ groups of [SH]. Error bars in i and I-o indicate s.d.

and Supplementary Section 1.2). The cells are short, with PHB granules (although unclear in transmission images) distinctively marked by PhaP1<sup>mV</sup>/PhaC<sup>mV</sup> fluorescence (Fig. 2c,d and Supplementary Fig. 10e,f). Compared with the non-adapted cells, these adapted cells also contain more PHB, which further increases at higher  $\rm H_2$  concentrations (Supplementary Fig. 11a); therefore, this PHB results from lithoautotrophic growth.

To visualize cellular MBH and SH, we tagged their respective subunits HoxG and HoxY with mV or the photoactivatable red fluorescent protein PAmCherry1 (PAmC1), where PAmC1 also enables single-molecule tracking and super-resolution imaging (Fig. 1d, mode II; note that different fluorescent tags show similar results, Supplementary Section 3). Confocal and wide-field fluorescence imaging both show that MBH $_{\rm HoxG}^{\rm PAmC1}$  is membrane-localized, as expected (Fig. 2e).

Single-molecule tracking of MBH  $^{PAmC1}_{HoxG}$  resolves a single diffusion state with a diffusion constant of  $1.67\pm0.07~\mu m^2~s^{-1}$  (Fig. 2g), typical of mobile membrane proteins  $^{28,29}$ . The  $H_2$ -oxidizing capability of MBH  $^{PAmC1}_{HoxG}$  is also indistinguishable from the non-tagged version (Supplementary Fig. 8). These findings support the tagged MBH being intact and functional in the cell. Surprisingly,  $SH^{mV}_{HoxY}$  (functionality confirmed in Supplementary Fig. 8g and Supplementary Table 3), besides being in the cytosol, also shows cell envelope localization (Fig. 2f), which we attribute to SH's interaction with inner-membrane or membrane-bound proteins, or its partial secretion to the periplasm, as some hydrogenases can be secreted out of cells  $^{30}$  (Fig. 4). Moreover, single-molecule tracking of  $SH^{PAmC1}_{HoxY}$  identified two diffusive states with diffusion constants of  $0.10\pm0.01$  and  $1.3\pm0.2~\mu m^2~s^{-1}$  (Fig. 2h), consistent with SH's multiple locations. Furthermore, both MBH and

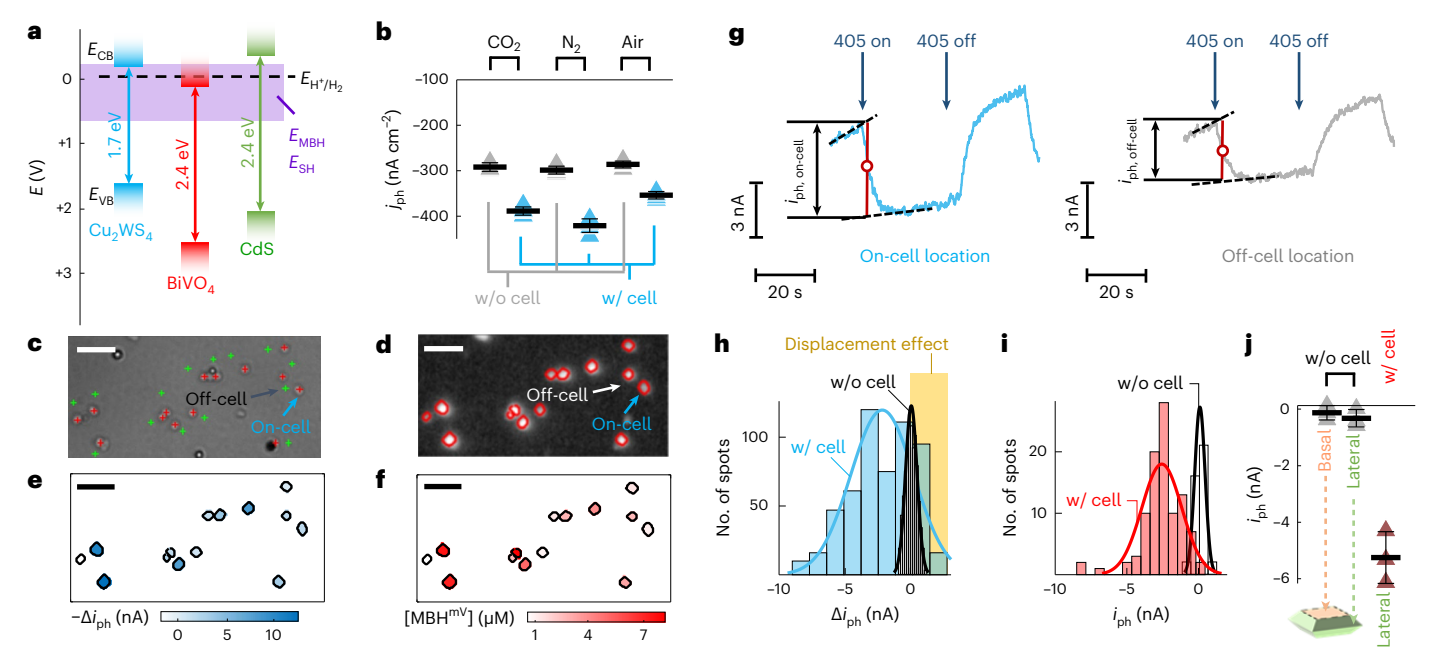


Fig. 3 | Electron uptake of R. eutropha from photoelectrodes in integrated biohybrids. a, Energy levels of the conduction band (CB) and valence band (VB) edges of Cu<sub>2</sub>WS<sub>4</sub>, BiVO<sub>4</sub> and CdS and the redox potential ranges (purple shade) of MBH (0.2 to 0.7 V) and SH (-0.02 to 0.1 V)<sup>23,38</sup>, all referenced to the RHE (H $^+$ /H<sub>2</sub>). **b**, Photoelectrochemical current densities at 0.2 V of a bulk Cu<sub>2</sub>WS<sub>4</sub> thin-film electrode with and without deposited multi-layer adapted R. eutropha cells in minimal medium under different gas environments (individual values are indicated by triangles). Horizontal black lines denote the mean. Error bars  $indicate \ s.d. \ from \ five \ on/off \ cycles. \ \boldsymbol{c}, Transmission \ image \ of \ adapted \ \textit{R. eutropha}$ cells encoding MBH<sup>mV</sup><sub>HoxG</sub> on a Cu<sub>2</sub>WS<sub>4</sub> film. Single-spot photocurrents were measured with a focused 405-nm laser illuminating at on-cell (red crosses) and nearby off-cell (green crosses) locations. d, Fluorescence image corresponding to  ${f c}$  (intensity is given in log scale to show contrast). Red lines show the cell contours. e, Colour-coded map of single-cell photocathodic current enhancement at 0.2 V, showing a correlation with local MBH concentration in f.  $\textbf{f}, Colour-coded\ map\ of\ MBH^{mV}_{HoxG}\ local\ concentration\ at\ the\ laser\ focus\ in\ each$ cell. **g**, Representative local photocurrent-time (i-t) trajectories at 0.2 V at an

on-cell location and its corresponding off-cell location under 405-nm light chopping, as denoted by arrows in  $\bf c$  and  $\bf d$ . Scale bars in  $\bf c$ - $\bf f$ , 5  $\mu$ m. Black dashed lines represent linear fitting of current before and after turning on light; the red lines with circle mark the time of the steepest change in current determined from the corresponding  $\Delta i/\Delta t$  trajectory (Supplementary Information Section 1.5). **h**, Histograms of single-cell  $\Delta i_{\rm ph}$  (blue) obtained on Cu<sub>2</sub>WS<sub>4</sub> (n = 511 cells) and a control  $Cu_2WS_4$  sample that contains no cells (black, n = 891 spots) at 0-0.3 V. For the control,  $\Delta i_{\rm ph}$  is between adjacent spots (Supplementary Section 1.5). The yellow shading denotes the cells whose intrinsic photocurrent is small and their overall  $\Delta i_{\rm ph}$  is positive due to dominance by the cell's displacement of water from the  $Cu_2WS_4$  surface. i, Histograms of  $i_{ph}$  obtained on single BiVO<sub>4</sub> particles with (red, n = 98 spots) and without (black, n = 41 spots) adapted R. eutropha at 0-0.3 V. Solid lines in **h-i** are Gaussian fits as guides to the eye. **j**, Comparison of  $i_{\rm ph}$  obtained on the cell-interfacing lateral facet, and on the cell-free lateral and basal facets of single BiVO<sub>4</sub> particles at 0.3 V (individual values are shown as triangles). Horizontal black lines denote the mean. Error bars indicate s.d. of measurements on three different particles contacting different cells.

SH cellular concentrations are upregulated by >20-fold upon adaptation (Fig. 2j), corroborating their importance in H<sub>2</sub> metabolism<sup>31</sup>.

Yet, we find that MBH and SH play different roles regarding PHB formation. Upon deleting MBH (that is,  $\Delta hoxG$ ), the PhaP1<sup>mV</sup> level stays unchanged, whereas deleting SH (that is,  $\Delta hoxY$ ) decreases the PhaP1<sup>mV</sup> level by -10<sup>3</sup> times (Fig. 2k, column 2 versus 1; 3 versus 1). Therefore, SH is critical for oxidizing H<sub>2</sub> to supply reducing equivalents (that is, NADH) towards PHB synthesis from CO<sub>2</sub> fixation (Fig. 4, steps (i) and (v)), while MBH is nonessential (but exhibits facilitating roles, as discussed in the following).

Genetic deletion does not inform, however, whether and how PHB production scales with SH level. To probe this, we tagged both SH  $_{\mbox{\scriptsize HoxY}}$  and PhaP1 with PAmC1 and mV, respectively, and quantified them via two-colour imaging in the same cell (Fig. 1c, mode l-ii). This double tagging does not affect PHB synthesis (Fig. 2k, column 5 versus 1), concurrently confirming that tagging HoxY does not affect its function. At the single-cell level, PhaP1 and SH levels show a clear positive correlation (Fig. 2l), consistent with the critical role of SH in PHB production and, more importantly, showing that more SH facilitates more PHB synthesis with  $\mbox{\scriptsize H}_2$  and  $\mbox{\scriptsize CO}_2$  lithoautotrophic growth.

In parallel, we tagged and imaged both MBH $_{HoxG}$  and PhaP1 in the same cell. Overall, the PhaP1 level stays the same, regardless of MBH tagging (Fig. 2k, column 4 versus 1). At the single-cell level, PhaP1 and

MBH levels also show a positive correlation (Fig. 2m), even though MBH is nonessential for PHB production. We attribute this correlation to the correlated MBH and SH expression (imaged by doubly tagging them; Fig. 2n), as both genes are regulated by the same regulatory hydrogenase (Supplementary Fig. 1c) $^{21,32}$ .

We wondered whether MBH's coexistence with SH could facilitate bioplastic formation. We therefore tagged PhaP1, MBH and SH with mV, mCherry (that is, mC) and PAmC1, respectively, and quantified them in the same cell. Here we combine wavelength and time separation to achieve three-channel imaging (Fig. 1c, mode I-iii): mV and mC are separated in wavelength, while PAmC1 and mC are separated in time utilizing PAmC1's photoactivation. Interestingly, in cells with an SH level of <1  $\mu$ M, PhaP1 level is independent of the cellular concentration ratio [MBH]/[SH] (Fig. 2o, yellow dots). However, when the SH level is higher, the PhaP1 level clearly increases with [MBH]/[SH] (Fig. 2o, blue/red dots), and this increase is not due to higher [SH] within each group (Supplementary Fig. 19). Therefore, although MBH is nonessential, it facilitates PHB production with SH present (Fig. 4, step i-a), and more so with higher SH levels.

#### Single-cell electron-uptake capability

Although *R. eutropha* was only employed in decoupled biohybrids (Fig. 1a, top)<sup>7</sup>, other lithoautotrophic bacteria have been interfaced directly with semiconductors to form integrated biohybrids for

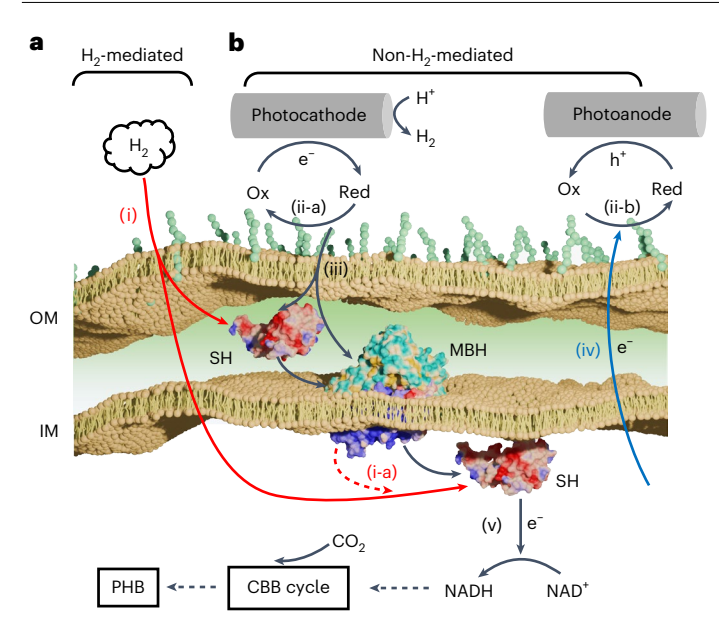


**Fig. 4** | Schematics of dominant electron-transport pathways for bioplastic formation in biohybrid systems. a, Under lithoautotrophic growth with  $H_2 + CO_2$  (that is, decoupled biohybrids),  $H_2$  gas enters a cell and is oxidized by SH (i), which provides electrons to generate NADH towards  $CO_2$  fixation for PHB synthesis through Calvin–Benson–Bassham (CBB) cycle (v); here, MBH has a facilitating role (i-a). **b**, At the microbe–semiconductor interface (that is, integrated biohybrids), electron uptake from the photocathode takes place dominantly via redox mediators (for example, possible flavin derivatives, secreted SH; ii-a) other than  $H_2$  and further passes to MBH and SH as required (iii), towards eventual  $CO_2$  fixation to PHB. Electron outflow to the photoanode is via redox mediators (ii-b), which may have overlapping species with ii-a (for example, possible flavin derivatives and so on), and does not require either SH or MBH (iv). OM, outer membrane; IM, inner membrane; Ox/Red, oxidized/reduced forms of redox mediators.

solar-to-fuel conversions (Fig. 1a, bottom) $^{9-11}$ . We therefore examined whether R. eutropha can accept electrons from photoelectrodes.

First, we interfaced R. eutropha with Cu<sub>2</sub>WS<sub>4</sub>, a photocathode material with visible absorption and a conduction band edge  $(E_{CR})$ appropriate for reducing protons, MBH, SH and other common cellular redox proteins such as NADH dehydrogenase and cytochrome c (Fig. 3a)<sup>23,33</sup>. Consistently, under 405-nm light excitation and an applied potential of 0.2 V (versus reversible hydrogen electrode (RHE) for all potentials cited here), Cu<sub>2</sub>WS<sub>4</sub> thin-film photoelectrodes alone show clear steady-state photocathodic currents from proton reduction in minimum medium (Fig. 3b, grey symbols), which is stable for >3 h (Supplementary Fig. 20). This photocathodic behaviour is independent of whether the environmental gas is  $N_2$ , air or  $CO_2$ , indicating indiscernible O<sub>2</sub> or CO<sub>2</sub> reduction on Cu<sub>2</sub>WS<sub>4</sub> under our conditions (Fig. 3b). Strikingly, upon depositing layers of adapted R. eutropha cells, steady-state photocathodic currents are enhanced (Fig. 3b, blue symbols), indicating that R. eutropha can take up electrons from Cu<sub>2</sub>WS<sub>4</sub>, either directly or via certain redox mediators. Such cell-induced photocathodic current enhancement exists across N2, air or CO2 environments (Fig. 3b), which is understandable, because the photocurrent (here, electron uptake) dominantly reflects upstream electron transfer near the cellsemiconductor interface rather than downstream cellular processes that involve electron movements (for example, respiration or CO<sub>2</sub> fixation). Control experiments on dead cells show no such photocurrent enhancement, indicating that this enhancement is specific to live cells (Supplementary Section 9).

Although our bulk measurements demonstrate the ability of *R. eutropha* to take up electrons, the multi-layer cell deposition makes

it challenging to quantify a single cell's electron-uptake capability, a key performance metric for microbe-semiconductor biohybrids. To quantify this, we integrated photoelectrochemical mapping into our multimodal imaging platform (Fig. 1e, mode III-i). We sparsely dispersed adapted R. eutropha cells on a Cu<sub>2</sub>WS<sub>4</sub> film on a transparent conductive indium tin oxide (ITO) substrate in a photoelectrochemical microfluidic cell (Supplementary Figs. 4 and 5h). With this arrangement, individual cells are easily identifiable in wide-field transmission and/or fluorescence images (Fig. 3c,d). A focused 405-nm laser (~380 nm in diameter) excites charge carriers locally in the semiconductor film and probes a single cell's current versus time (i-t) response under light chopping at various applied potentials. This laser illumination does not cause a noticeable change in a cell's photoelectrochemical behaviour or morphology (Supplementary Section 10). A typical single-cell *i-t* response shows a greater photocathodic current ( $i_{ph}$ ) than that measured at an adjacent location on the semiconductor film (Fig. 3g, left versus right, Fig. 3c and Supplementary Fig. 21); the difference,  $\Delta i_{\rm ph}$ , directly yields an individual cell's photocurrent contribution, a single-celllevel photoelectrochemical measurement.

We measured  $\Delta i_{\rm ph}$  for many cells. In the narrow range of 0–0.3 V,  $\Delta i_{\rm ph}$  has no discernible potential dependence (Supplementary Fig. 23a). The majority (~77%) of the cells show photocathodic current enhancement (that is,  $\Delta i_{ph}$  < 0; Fig. 3h, blue), consistent with bulk measurements (Fig. 3b). The remaining minor population (~23%) have  $\Delta i_{ph} > 0$ , and we attribute this behaviour to the cell's displacement of water from the Cu<sub>2</sub>WS<sub>4</sub> surface, leading to suppressed proton reduction that dominates over these cells' photocathodic currents (Supplementary Section 8). Importantly, the single-cell photocathodic currents  $\Delta i_{ph}$  average at  $-2.2 \pm 0.2$  nA, which, surprisingly, is ~103 times larger than the picoampere-level current that cellular hydrogenases are capable of sustaining via H<sub>2</sub>-mediated electron transport (Supplementary Section 11.1).  $\Delta i_{\rm ph}$  due to semiconductor film heterogeneity is only 0.07 ± 0.03 nA (Fig. 3h, black). This large single-cell photocurrent enhancement suggests that either the turnover rates of the hydrogenases were underestimated, or other non-H<sub>2</sub>-mediated electron-transport pathways dominate the cell's photocathodic current here.

To probe the mechanisms underlying these large single-cell photocurrents, we eliminated the  $H_2$ -mediated electron transport by attaching cells to BiVO<sub>4</sub> with  $E_{CB}$  below the proton reduction potential (Fig. 3a)<sup>34</sup>. Using a focused 405-nm laser, we measured local photocurrents on the lateral facets of individual micrometre-sized BiVO<sub>4</sub> particles (Fig. 1e, mode III-ii; Supplementary Fig. 6a). As expected, BiVO<sub>4</sub> particles alone show no photocathodic current at 0.2 V (Fig. 3i, black; Supplementary Fig. 25). Remarkably, BiVO<sub>4</sub> particles surrounded by adapted *R. eutropha* cells exhibit clear photocathodic currents at  $-2.6 \pm 0.3$  nA (Fig. 3i, red; Supplementary Fig. 26). Therefore, non- $H_2$ -mediated electron-transport pathways indeed exist in *R. eutropha*, and probably dominate the nanoampere-level single-cell photocathodic current on  $Cu_2WS_4$  (Fig. 4, step ii-a).

To remove complications from particle-to-particle and cell-to-cell variations in our BiVO<sub>4</sub>/cell measurements, we further implemented single-cell, single-particle photocurrent measurement by interfacing larger-sized non-adapted *R. eutropha* cells with BiVO<sub>4</sub> particles with facets larger than the focused laser (Fig. 1e, mode III-iii). The single-cell/single-particle interface is easily identifiable (Supplementary Figs. 5f and 6b), and the focused laser can be placed at different sub-BiVO<sub>4</sub>-particle locations. When the laser focus is on a particle's lateral facet that contacts a cell, a photocathodic current (–5.3  $\pm$  0.9 nA) is clear (Fig. 3j). In contrast, no appreciable photocathodic current is observed when the laser is at another cell-free lateral or a basal facet of the same particle (Fig. 3j). These single-cell/single-particle results corroborate the existence of non-H<sub>2</sub>-mediated semiconductor-to-cell electron-transport pathways.

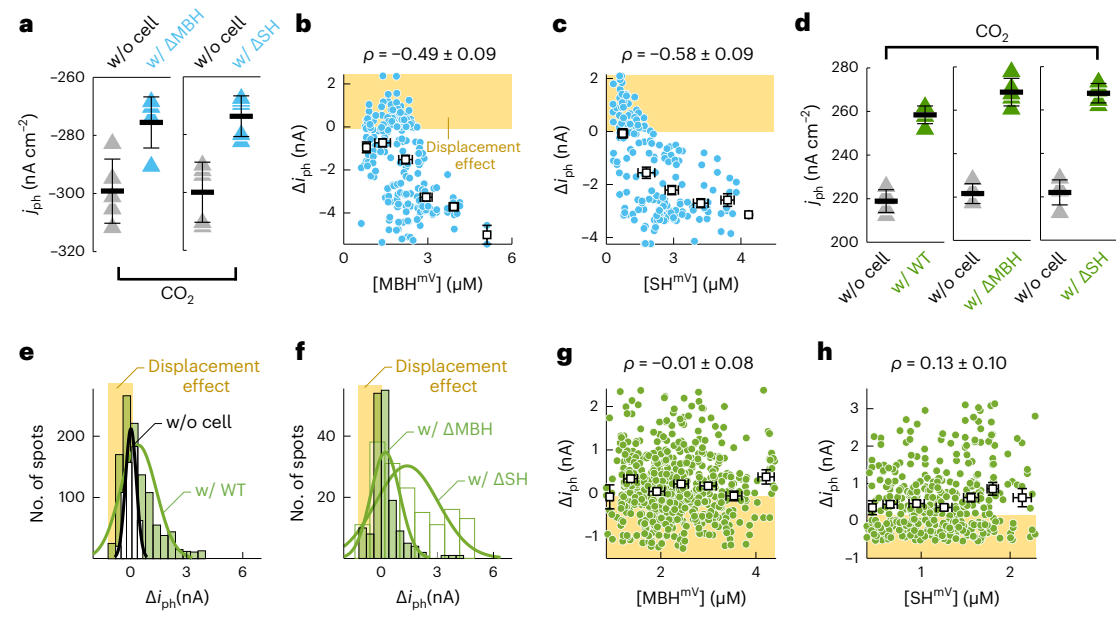


Fig. 5 | Players in electron transport across the microbe–semiconductor interface. a, Photoelectrochemical current densities at 0.2 V of bulk  $Cu_2WS_4$  thin-film photocathodes with and without deposited multi-layer adapted R. eutropha  $\Delta$ MBH (that is,  $\Delta hoxG$ ) or  $\Delta$ SH (that is,  $\Delta hoxY$ ) cells in minimum medium under a  $CO_2$  environment (individual values are shown as triangles). Horizontal black lines denote the mean. Error bars indicate s.d. of five on/off cycles. **b,c**, Correlations of single-cell  $\Delta i_{\rm ph}$  obtained on a  $Cu_2WS_4$  photocathode at 0–0.3 V with local MBH (**b**) or SH (**c**) concentration at the laser focus of the same cell. Blue dots, individual adapted cells. Open squares, binned and averaged results. Yellow shaded areas indicate cells with lower hydrogenase levels that are dominated by the displacement effect, similar to Fig. 3h (same for **e-h**).

x error bars indicate s.d. y error bars indicate s.e.m. n = 230 cells (**b**), 194 cells (**c**). **d**, Photoelectrochemical current densities at 1.1 V of bulk CdS thin-film photoelectrodes with and without deposited multi-layer adapted R. eutropha WT or single-deletion cells in minimum medium under a  $CO_2$  environment (individual values are shown as triangles). Horizontal black lines denote the mean. Error bars indicate s.d. of five on/off cycles. **e**, Histograms of single-cell  $\Delta i_{\rm ph}$  of WT adapted R. eutropha on CdS thin-film photoelectrodes (green) and a control CdS photoelectrode without cells (black) at 0.7–1.0 V ( $\Delta i_{\rm ph}$  has no discernible potential dependence in this range; Supplementary Fig. 23b). Solid lines are Gaussian fits as guides to the eye. **f**, As in **e** but using adapted  $\Delta$ MBH and  $\Delta$ SH strains. **g**, **h**, As in **b**, **c**, but on CdS photoanodes at 0.7–1.0 V. Source data

#### Interfacial electron-transport pathways

Hydrogenases, besides metabolizing  $H_2$ , have been proposed to possibly participate in electron transport involving other redox mediators  $^{10}$ . Our discovery of non- $H_2$ -mediated electron-transport pathways between R. eutropha and semiconductors prompted us to examine the role of hydrogenases in such pathways. We first examined the bulk photoelectrochemical properties of adapted  $\Delta$ MBH and  $\Delta$ SH strains on thin-film  $Cu_2WS_4$  photocathodes. Remarkably, neither deletion strain shows the photocathodic current enhancement present in the wild-type (WT) strain (Fig. 5a versus Fig. 3b), indicating that both MBH and SH play critical roles in sustaining electron uptake across the microbe–semiconductor interface (Fig. 4, step iii). For MBH, this role is consistent with it being an inner-membrane protein. For SH, we attribute this role at least in part to it being recruited to the membrane and/or secreted into the periplasm (Figs. 2f and 4).

To quantify the contribution of MBH and SH to the cell-induced photocathodic enhancement  $(\Delta i_{\rm ph})$ , we examined single-cell-level correlations between a cell's hydrogenase levels and  $\Delta i_{\rm ph}$  by combining wide-field fluorescence imaging and single-spot photocurrent measurements for adapted cells on Cu<sub>2</sub>WS<sub>4</sub> (Fig. 1c,e, mode I-i and III-i). A clear correlation exists between  $\Delta i_{\rm ph}$  and cellular hydrogenase levels; that is, the magnitude of  $\Delta i_{\rm ph}$  increases with increasing local cellular MBH and SH concentrations (Figs. 3e,f and 5b,c). Therefore, higher hydrogenase levels are associated with a stronger electron-uptake capability in cells, corroborating the critical role of both MBH and SH in sustaining semiconductor-to-microbe electron transport.

However, because neither MBH nor SH is normally on the outer membrane, they are not expected to be in direct contact with the photoelectrode to accept photogenerated electrons. We hypothesized that there must be redox mediators at the *R. eutropha* surface (for example,

outer membrane and/or extracellular matrix) to shuttle electrons from the photoelectrodes to the hydrogenases. These mediators should include but not be dominated by  $H^+/H_2$  based on our results above. To probe potential cell-surface redox mediators, we performed bulk cyclic voltammetry on the supernatant of the adapted cell cultures and identified a catalytic species (possibly secreted SH) as well as two other redox species that could be flavin derivatives (Supplementary Section 12.1). Importantly, to sustain steady-state semiconductor-to-microbe currents, these mediators must be redox-reversible and hence should also be able to mediate anodic, microbe-to-semiconductor electron transport (Fig. 4, step ii-b).

Therefore, to test our hypothesis and probe such cell-surface redox mediators, we interfaced R. eutropha with CdS, a typical photoanode material excitable by 405-nm light (Fig. 3a)<sup>35</sup>. On bulk thin-film CdS photoelectrodes with layers of adapted WT cells, cell-induced photoanodic current enhancement is indeed observed (Fig. 5d, left), confirming the reversibility of such redox mediators. Interestingly, for the  $\Delta$ MBH and  $\Delta$ SH strains, this cell-induced photoanodic current enhancement persists (Fig. 5d, middle and right), indicating that both types of hydrogenase are not important for electron outflow (Fig. 4, step iv).

We also performed single-cell measurements on CdS photoanodes to eliminate cell-density heterogeneities in the bulk measurements. Most WT cells exhibit pronounced photoanodic current enhancement ( $\Delta i_{ph}$  of a few nanoamperes; Fig. 5e, green), consistent with bulk measurements (Fig. 5d). A minor population shows photoanodic current suppression ( $\Delta i_{ph} < 0$ ; Fig. 5e), again attributable to the water displacement effect that is only apparent for single-cell-level measurements and is applicable to both photocathodic and photoanodic behaviours.  $\Delta i_{ph}$  due to CdS film heterogeneity is small, at  $0.02 \pm 0.03$  nA (Fig. 5e, black).

The  $\Delta$ MBH and  $\Delta$ SH strains show comparable  $\Delta i_{ph}$  values (Fig. 5f versus 5e), consistent with the bulk-level comparison across different strains (Fig. 5d). Moreover, single-cell  $\Delta i_{ph}$  does not show notable correlation with either MBH or SH local concentration (Fig. 5g,h). These results corroborate that MBH and SH do not play important roles in electron outflow. Altogether, at the microbe–semiconductor interface, the cell-surface non-H<sub>2</sub>-based redox mediators are important for both electron outflow and electron uptake (Fig. 4, steps ii-a and ii-b), whereas MBH and SH are important only for electron uptake (Fig. 4, step iii).

#### **Conclusions**

Microbe-semiconductor biohybrids hold promise for efficient solar-to-chemical conversion. We have demonstrated that R. eutropha can (1) metabolize H<sub>2</sub> for bioplastic synthesis from CO<sub>2</sub> in decoupled biohybrids, with MBH and SH assuming different roles, and (2) take up electrons efficiently from photoelectrodes via non-H<sub>2</sub>-mediated pathways, with both hydrogenases being crucial. This raises the possibility of using R. eutropha in both decoupled and integrated microbe-semiconductor biohybrids, or even synergistically combined, to harvest sunlight to synthesize value-added chemicals. The large electron-uptake capability of R. eutropha highlights the potential to leverage synthetic biology to direct more electrons towards bioplastic production in the cell, for example by engineering the protein expression, linkage and kinetics of electron-transport pathways and carbon-fixation cycles. Overall, our non-invasive multimodal imaging approach uncovers valuable mechanistic information down to single-cell resolution, and can identify species critical for electron transport and assess system performance, with enhanced capabilities if further integrated with other tools like NanoSIMS<sup>36,37</sup> and proteomics. The knowledge can also guide the engineering and optimization of diverse biohybrid systems for many types of process, including CO<sub>2</sub> fixation, N<sub>2</sub> fixation and pollutant degradation.

#### **Online content**

Any methods, additional references, Nature Portfolio reporting summaries, source data, extended data, supplementary information, acknowledgements, peer review information; details of author contributions and competing interests; and statements of data and code availability are available at https://doi.org/10.1038/s41557-023-01285-z.

#### References

- Cestellos-Blanco, S., Zhang, H., Kim, J. M., Shen, Y. X. & Yang, P. Photosynthetic semiconductor biohybrids for solar-driven biocatalysis. *Nat. Catal.* 3, 245–255 (2020).
- Rabaey, K. & Rozendal, R. A. Microbial electrosynthesis—revisiting the electrical route for microbial production. *Nat. Rev. Microbiol.* 8, 706–716 (2010).
- Kracke, F., Vassilev, I. & Krömer, J. O. Microbial electron transport and energy conservation—the foundation for optimizing bioelectrochemical systems. Front. Microbiol. 6, 575 (2015).
- Kornienko, N., Zhang, J. Z., Sakimoto, K. K., Yang, P. & Reisner, E. Interfacing nature's catalytic machinery with synthetic materials for semi-artificial photosynthesis. *Nat. Nanotechnol.* 13, 890–899 (2018).
- Dogutan, D. K. & Nocera, D. G. Artificial photosynthesis at efficiencies greatly exceeding that of natural photosynthesis. Acc. Chem. Res. 52, 3143–3148 (2019).
- Nangle, S. N., Sakimoto, K. K., Silver, P. A. & Nocera, D. G. Biological-inorganic hybrid systems as a generalized platform for chemical production. *Curr. Opin. Chem. Biol.* 41, 107–113 (2017).
- Liu, C., Colón, B. C., Ziesack, M., Silver, P. A. & Nocera, D. G. Water splitting-biosynthetic system with CO<sub>2</sub> reduction efficiencies exceeding photosynthesis. Science 352, 1210–1213 (2016).
- 8. Nichols, E. M. et al. Hybrid bioinorganic approach to solar-to-chemical conversion. *Proc. Natl Acad. Sci. USA* **112**, 11461–11466 (2015).

- Liu, C. et al. Nanowire-bacteria hybrids for unassisted solar carbon dioxide fixation to value-added chemicals. Nano Lett. 15, 3634–3639 (2015).
- Sakimoto, K. K., Wong Andrew, B. & Yang, P. Self-photosensitization of nonphotosynthetic bacteria for solar-to-chemical production. Science 351, 74–77 (2016).
- Wang, B., Jiang, Z., Yu, J. C., Wang, J. & Wong, P. K. Enhanced CO<sub>2</sub> reduction and valuable C<sub>2+</sub> chemical production by a CdSphotosynthetic hybrid system. *Nanoscale* 11, 9296–9301 (2019).
- 12. Guo, J. et al. Light-driven fine chemical production in yeast biohybrids. Science **362**, 813–816 (2018).
- Kornienko, N. et al. Spectroscopic elucidation of energy transfer in hybrid inorganic-biological organisms for solar-to-chemical production. *Proc. Natl Acad. Sci. USA* 113, 11750–11755 (2016).
- Brown Katherine, A. et al. Light-driven dinitrogen reduction catalyzed by a CdS:nitrogenase MoFe protein biohybrid. Science 352, 448–450 (2016).
- Dong, F., Lee, Y. S., Gaffney, E. M., Liou, W. & Minteer, S. D. Engineering cyanobacterium with transmembrane electron transfer ability for bioelectrochemical nitrogen fixation. ACS Catal. 11, 13169–13179 (2021).
- Knoche, K. L., Aoyama, E., Hasan, K. & Minteer, S. D.
  Role of nitrogenase and ferredoxin in the mechanism of
  bioelectrocatalytic nitrogen fixation by the cyanobacteria
  Anabaena variabilis SA-1 mutant immobilized on indium tin oxide
  (ITO) electrodes. Electrochim. Acta 232, 396–403 (2017).
- Taniguchi, Y. et al. Quantifying E. coli proteome and transcriptome with single-molecule sensitivity in single cells. Science 329, 533–538 (2010).
- Debroye, E. et al. Facet-dependent photoreduction on single ZnO crystals. J. Phys. Chem. Lett. 8, 340–346 (2017).
- Mao, X. & Chen, P. Inter-facet junction effects on particulate photoelectrodes. *Nat. Mater.* 21, 331–337 (2021).
- Reinecke, F. & Steinbüchel, A. Ralstonia eutropha strain H16 as model organism for PHA metabolism and for biotechnological production of technically interesting biopolymers. J. Mol. Microbiol. Biotechnol. 16, 91–108 (2009).
- Burgdorf, T. et al. [NiFe]-hydrogenases of Ralstonia eutropha H16: modular enzymes for oxygen-tolerant biological hydrogen oxidation. J. Mol. Microbiol. Biotechnol. 10, 181–196 (2005).
- Pohlmann, A. et al. Genome sequence of the bioplastic-producing 'Knallgas' bacterium *Ralstonia eutropha* H16. Nat. Biotechnol. 24, 1257–1262 (2006).
- Cramm, R. Genomic view of energy metabolism in Ralstonia eutropha H16. J. Mol. Microbiol. Biotechnol. 16, 38–52 (2009).
- Pötter, M. et al. The complex structure of polyhydroxybutyrate (PHB) granules: four orthologous and paralogous phasins occur in *Ralstonia eutropha*. *Microbiology* 150, 2301–2311 (2004).
- Peoples, O. P. & Sinskey, A. J. Poly-P-hydroxybutyrate (PHB) biosynthesis in *Alcaligenes eutrophus* H16. J. Biol. Chem. 264, 15298–15303 (1989).
- Bresan, S. et al. Polyhydroxyalkanoate (PHA) granules have no phospholipids. Sci. Rep. 6, 26612 (2016).
- York, G. M., Junker, B. H., Stubbe, J. & Sinskey, A. J. Accumulation of the PhaP phasin of *Ralstonia eutropha* is dependent on production of polyhydroxybutyrate in cells. *J. Bacteriol.* 183, 4217–4226 (2001).
- Fu, B. et al. Metal-induced sensor mobilization turns on affinity to activate regulator for metal detoxification in live bacteria. *Proc. Natl Acad. Sci. USA* 117, 13248–13255 (2020).
- Mullineaux, C. W., Nenninger, A., Ray, N. & Robinson, C. Diffusion of green fluorescent protein in three cell environments in Escherichia coli. J. Bacteriol. 188, 3442–3448 (2006).
- Deutzmann, J. S., Sahin, M., Spormann, A. M. & Harwood, C. S. Extracellular enzymes facilitate electron uptake in biocorrosion and bioelectrosynthesis. mBio 6, e00496–00415 (2015).

- Kohlmann, Y. et al. Analyses of soluble and membrane proteomes of *Ralstonia eutropha* H16 reveal major changes in the protein complement in adaptation to lithoautotrophy. *J. Proteome Res.* 10, 2767–2776 (2011).
- 32. Friedrich, B., Buhrke, T., Burgdorf, T. & Lenz, O. A hydrogen-sensing multiprotein complex controls aerobic hydrogen metabolism in *Ralstonia eutropha. Biochem. Soc. Trans.* 33, 97–101 (2005).
- 33. Aslan, E. et al. Photocatalytic  $H_2$  evolution with a  $Cu_2WS_4$  catalyst on a metal free D- $\pi$ -A organic dye-sensitized  $TiO_2$ . *Appl. Catal. B* **210**, 320–327 (2017).
- Sivula, K. & van de Krol, R. Semiconducting materials for photoelectrochemical energy conversion. *Nat. Rev. Mater.* 1, 15010 (2016).
- Nasir, J. A. et al. Recent developments and perspectives in CdS-based photocatalysts for water splitting. J. Mater. Chem. A 8, 20752–20780 (2020).
- Lanni, E. J. et al. Correlated imaging with C60-SIMS and confocal Raman microscopy: visualization of cell-scale molecular distributions in bacterial biofilms. *Anal. Chem.* 86, 10885–10891 (2014).

- Chadwick, G. L., Jiménez, O. F., Gralnick, J. A., Bond, D. R. & Orphan, V. J. NanoSIMS imaging reveals metabolic stratification within current-producing biofilms. *Proc. Natl Acad. Sci. USA* 116, 20716–20724 (2019).
- 38. Saggu, M. et al. Spectroscopic insights into the oxygen-tolerant membrane-associated [NiFe] hydrogenase of *Ralstonia eutropha* H16. *J. Biol. Chem.* **284**, 16264–16276 (2009).

**Publisher's note** Springer Nature remains neutral with regard to jurisdictional claims in published maps and institutional affiliations.

Springer Nature or its licensor (e.g. a society or other partner) holds exclusive rights to this article under a publishing agreement with the author(s) or other rightsholder(s); author self-archiving of the accepted manuscript version of this article is solely governed by the terms of such publishing agreement and applicable law.

@ The Author(s), under exclusive licence to Springer Nature Limited 2023

#### Methods

## Strain construction, growth condition and semiconductor material synthesis

All genetic engineering, including fluorescent protein tagging and gene knockout, was done using the biparental conjugation method<sup>39</sup>. Briefly, for tagging, the conjugation plasmid was constructed by Gibson assembly of HR1, HR2 and the fluorescent protein gene into pRE118 vector, where HR1 and HR2 are the 1,000-bp regions flanking upstream and downstream of the stop codon of the target gene (HoxG, HoxY or *PhaP1*), respectively. For gene knockout, only HR1 and HR2 were cloned into the conjugation vector, where HR1 and HR2 are regions flanking upstream and downstream of the entire target gene. The conjugation plasmid was transformed into donor Escherichia coli strain WM3064, which was then conjugated with R. eutropha. Colonies with correct double crossover were screened by PCR and sequence-confirmed. R. eutropha was routinely grown in tryptic soy broth (TSB) overnight at 30 °C, then diluted in minimum medium supplemented with 1% wt/vol fructose for two days. These cells are termed non-adapted cells throughout the Article. For adaptation to the lithoautotrophic condition, non-adapted cells were diluted to an optical density of 0.2 in minimum medium and further grown under H2:CO2 (4:1, total 9% or 30%, balanced with air) for four days  $^{40}$ . These cells are termed adapted cells. Details are provided in Supplementary Section 1.2.

All three semiconductor particles (CdS, Cu $_2$ WS $_4$  and BiVO $_4$ ) were synthesized in house using hydrothermal methods. The CdS nanoparticles are nanorods with width of ~50 nm and length of ~1 µm. The Cu $_2$ WS $_4$  and BiVO $_4$  particles have truncated bipyramid shapes with sizes varying between 1 µm and 10 µm, respectively. Details are provided in Supplementary Section 1.1 and scanning electron microscopy (SEM) characterization is provided in Supplementary Fig. 5.

#### Optical imaging and photoelectrochemical measurements

For the imaging of bacteria without semiconductor, cells were dispersed and immobilized between a glass coverslip and an agarose pad<sup>28</sup>. The sample edges were sealed with epoxy to prevent gel drying. Single-molecule tracking and single-cell protein quantification were performed with a ×60 oil immersion objective (Olympus PlanApo N ×60 oil 1.45 TIRFM UIS 2) on an Olympus IX71 inverted microscope, and the images were captured with an electron-multiplying charge-coupled device (EMCCD) camera (Andor Technology, DU-897E-CSO-#BV). The total magnification was ×115, which leads to a pixel size of 135.4 nm (ref. 41). The circularly polarized continuous-wave lasers were aligned coaxially and inclined at approximately 60° from the optical axis of the objective to decrease background from the medium. mCherry was excited by 561 nm, mVenus by 514 nm, and PAmCherry1 was first activated by 405 nm and then excited by 561 nm. The emission light was collected by the EMCCD camera after passing through appropriate bandpass filters. Single-molecule tracking was done in stroboscopic mode, with a 4-ms laser pulse controlled by an acousto-optic tunable filter and a time lag for each camera frame of 60 ms. The short laser pulse minimized motion blur from the fast movement of proteins. For protein quantification of multiple tagged strains, different proteins were imaged sequentially in the order (1) mCherry, (2) mVenus and (3) PAmCherry1. Details are provided in Supplementary Section 1.3 and Fig. 1b.

For bulk-level photoelectrochemical measurements on annealed semiconductor thin-film electrodes, a three-electrode set-up was used. A Pt wire electrode (BASi, MW-4139) and a Ag/AgCl electrode (BASi, MW-2030) were used as counterelectrode and reference electrode, respectively. For no-cell control experiments, the annealed electrodes were mounted in a quartz cell filled with minimum medium and held at a constant potential. The 405-nm laser was kept on for a duration of 15 s and off for a duration of 10 s while the photocurrent was recorded. A large amount of adapted  $R.\ eutropha$  cells were then deposited on the same semiconductor electrode and immobilized with an agarose pad

and a coverslip. The photocurrent was measured again in the presence of cells under exactly the same condition.

For multimodal imaging of single cells coupled with semiconductor films (Cu<sub>2</sub>WS<sub>4</sub> and CdS), a three-electrode photoelectrochemical microfluidic cell was constructed. Semiconductor-deposited ITO was attached to two glass slides and R. eutropha cells were dispersed on the semiconductor film surface. The cells were sandwiched between the ITO electrode and another microscope slide by an agarose pad. A Pt wire counterelectrode and a Ag/AgCl reference electrode were assembled into the microfluidic structure, which was then sealed with epoxy to prevent leaking. Minimal medium was introduced into the device by a syringe. The sample was imaged on an inverted Olympus IX71 microscope equipped with a ×60 water immersion objective (Olympus, UPLSAPO60XW) to image through the agarose pad. Cells in the field of view were first imaged and bleached by wide-field laser excitation for protein quantification. Then, a focused 405-nm laser beam was directed to each single cell for the measurement of photocurrent at that location. Photocurrent from a nearby off-cell location was also measured as a control. In the case of BiVO<sub>4</sub>, a single nanoparticle instead of nanoparticle film was used. Focused 405 nm light was directed onto the basal or lateral facet of the BiVO<sub>4</sub>. For details see Supplementary Section 1.5 and Supplementary Figs. 4 and 6.

#### Analysis of images and photocurrents

Single-cell protein quantification was calculated as the whole-cell fluorescence intensity divided by the single fluorescent protein intensity. The fluorescence bleaching curve was fitted to a double exponential decay function, where one component corresponds to fluorescent protein bleaching and the other to cell autofluorescence. Off-cell background and cell autofluorescence were subtracted. Details are provided in Supplementary Section 1.4. Protein dynamic information is extracted by fitting the displacement distribution from single-molecule tracking to a multi-state probability distribution function, and the cell-confinement effect is resolved through an inverse transformation algorithm. Details are provided in Supplementary Section 7.

To quantify the photocurrent, currents for the two 3-s durations on either side of the time of turning illumination on,  $(t_{\rm on}-4\,{\rm s},t_{\rm on}-1\,{\rm s})$  and  $(t_{\rm on}+1\,{\rm s},t_{\rm on}+4\,{\rm s})$ , were fitted with two different linear functions, and the difference between these two linear functions at  $t_{\rm on}$  was taken as the photocurrent (that is,  $i_{\rm ph}$ ) for this light on/off cycle. Details are provided in Supplementary Section 1.5.

#### **Reporting summary**

Further information on research design is available in the Nature Portfolio Reporting Summary linked to this article.

#### **Data availability**

All data are available in the main text or the Supplementary Information. Raw data supporting the findings of this study are available upon reasonable request. Source data are provided with this paper.

#### **Code availability**

MATLAB codes for data analysis and simulations supporting the findings of this study are provided with this paper.

#### References

- Edwards, R. A., Keller, L. H. & Schifferli, D. M. Improved allelic exchange vectors and their use to analyze 987P fimbria gene expression. *Gene* 207, 149–157 (1998).
- Torella, J. P. et al. Efficient solar-to-fuels production from a hybrid microbial-water-splitting catalyst system. *Proc. Natl Acad. Sci.* USA 112, 2337–2342 (2015).
- Chen, T.-Y. et al. Concentration- and chromosome-organizationdependent regulator unbinding from DNA for transcription regulation in living cells. *Nat. Commun.* 6, 7445 (2015).

#### Acknowledgements

This research is supported by the US Department of Energy (Office of Science, Office of Biological and Environmental Research, Biological Systems Science Division, under award no. DE-SC0020179). It uses Cornell Center for Materials Research Shared Facilities supported through the NSF MRSEC programme (DMR-1719875). The funders had no role in study design, data collection and analysis, decision to publish or preparation of the manuscript. We thank C. Brigham at Wentworth Institute of Technology for providing the *R. eutropha* H16 strain, W. Metcalf at the University of Illinois at Urbana Champaign for *E. coli* WM3064, O. Lenz at Technische Universität Berlin for *R. eutropha* ΔhoxH, L. Krzeminski formerly at Cornell University for constructing tagged *E. coli* strains, and S. Murphy, T. Doerr and A. Schmitz at Cornell University for discussions on genetics.

#### **Author contributions**

B.F. constructed strains. X.M. synthesized semiconductor materials. B.F. and X.M. designed experiments, performed measurements, wrote codes and analysed data. Y.P., Z.Z. and T.Y. contributed to strain construction, materials synthesis and/or imaging experiments, where Y.P. and Z.Z. contributed equally. W.J. and D.H.F. contributed

to cell culturing. W.L. helped with instrument set-up. B.P., F.S. and B.B. contributed to genetic engineering. M.S. and T.H. contributed to discussions on materials synthesis. P.C. conceived and directed the research. B.F., X.M. and P.C. wrote the manuscript.

#### **Competing interests**

The authors declare no competing interests.

#### **Additional information**

**Supplementary information** The online version contains supplementary material available at https://doi.org/10.1038/s41557-023-01285-z.

**Correspondence and requests for materials** should be addressed to Peng Chen.

**Peer review information** *Nature Chemistry* thanks the anonymous reviewers for their contribution to the peer review of this work.

**Reprints and permissions information** is available at www.nature.com/reprints.

# nature portfolio

Corresponding author(s):	Peng Chen
Last updated by author(s):	May 27, 2023

## **Reporting Summary**

Nature Portfolio wishes to improve the reproducibility of the work that we publish. This form provides structure for consistency and transparency in reporting. For further information on Nature Portfolio policies, see our <u>Editorial Policies</u> and the <u>Editorial Policy Checklist</u>.

For all statistical analyses, confirm that the following items are present in the figure legend, table legend, main text, or Methods section.

$\overline{}$				
Ç.	tっ	1	ıct.	CC
ാ	La	L	ist	いしろ

n/a	Confirmed		
	The exact sample size (n) for each experimental group/condition, given as a discrete number and unit of measurement		
	🔀 A statement on whether measurements were taken from distinct samples or whether the same sample was measured repeatedly		
	The statistical test(s) used AND whether they are one- or two-sided Only common tests should be described solely by name; describe more complex techniques in the Methods section.		
	A description of all covariates tested		
$\boxtimes$	A description of any assumptions or corrections, such as tests of normality and adjustment for multiple comparisons		
	A full description of the statistical parameters including central tendency (e.g. means) or other basic estimates (e.g. regression coefficient) AND variation (e.g. standard deviation) or associated estimates of uncertainty (e.g. confidence intervals)		
	For null hypothesis testing, the test statistic (e.g. <i>F</i> , <i>t</i> , <i>r</i> ) with confidence intervals, effect sizes, degrees of freedom and <i>P</i> value noted <i>Give P values as exact values whenever suitable.</i>		
$\boxtimes$	For Bayesian analysis, information on the choice of priors and Markov chain Monte Carlo settings		
$\boxtimes$	For hierarchical and complex designs, identification of the appropriate level for tests and full reporting of outcomes		
	$\boxtimes$ Estimates of effect sizes (e.g. Cohen's $d$ , Pearson's $r$ ), indicating how they were calculated		
,	Our web collection on <u>statistics for biologists</u> contains articles on many of the points above.		
Software and code			
Polic	ry information about <u>availability of computer code</u>		

#### Data collection

Super-resolution/wide-field fluorescence and transmission images were collected with Andor iQ2 software; photocurrent data was collected with software CH1200A Electrochemical Analyzer; confocal images were collected with ZEN software. All the above information are described in the main text or SI.

Data analysis

Customized MATLAB\_R2021a codes were used for data analysis, which are provided by the authors.

For manuscripts utilizing custom algorithms or software that are central to the research but not yet described in published literature, software must be made available to editors and reviewers. We strongly encourage code deposition in a community repository (e.g. GitHub). See the Nature Portfolio guidelines for submitting code & software for further information.

#### Data

Policy information about availability of data

All manuscripts must include a data availability statement. This statement should provide the following information, where applicable:

- Accession codes, unique identifiers, or web links for publicly available datasets
- A description of any restrictions on data availability
- For clinical datasets or third party data, please ensure that the statement adheres to our policy

All data are available in the main text or the supplementary materials. Raw data supporting the findings of this study are available upon reasonable request.

Human research participants						
Policy information about studies involving human research participants and Sex and Gender in Research.						
Reporting on sex	and gender	N/A				
Population characteristics		N/A				
Recruitment N/A		N/A				
Ethics oversight		N/A				
Note that full informa	ation on the appr	oval of the study protocol must also be provided in the manuscript.				
Field-spe		porting s the best fit for your research. If you are not sure, read the appropriate sections before making your selection.				
X Life sciences		ehavioural & social sciences Ecological, evolutionary & environmental sciences				
For a reference copy of t	the document with	all sections, see <u>nature.com/documents/nr-reporting-summary-flat.pdf</u>				
Life scier	nces sti	udy design				
All studies must dis	close on these	points even when the disclosure is negative.				
Sample size	_	neasurement, enough data (> 60 cells for each condition) were compiled to ensure statistical significance. We find that such ufficient to form a smooth distribution and represent data trend.				
Data exclusions	When outliers	exist, data outside 95 percentile were excluded, which is sufficient to exclude extreme outliers in our case.				
Replication	Replications were successful and data from same conditions were combined together. Each condition includes at least three repetitions, which are comparable with each other.					
Randomization	Not relevant as no allocation was performed.					
Blinding	Not relevant as no grouping was performed.					
Reporting for specific materials, systems and methods  We require information from authors about some types of materials, experimental systems and methods used in many studies. Here, indicate whether each material, system or method listed is relevant to your study. If you are not sure if a list item applies to your research, read the appropriate section before selecting a response.						
system of meaning about the your stady, if you are not sure if a list term applies to your research, read the appropriate section before selecting a response.						
Materials & experimental systems Methods						
n/a   Involved in the study						

Materials & experimental systems		Methods	
n/a	Involved in the study	n/a	Involved in the study
$\boxtimes$	Antibodies	$\boxtimes$	ChIP-seq
$\boxtimes$	Eukaryotic cell lines	$\boxtimes$	Flow cytometry
$\boxtimes$	Palaeontology and archaeology	$\boxtimes$	MRI-based neuroimaging
$\boxtimes$	Animals and other organisms		•
$\boxtimes$	Clinical data		
$\boxtimes$	Dual use research of concern		